optica

Polarization-sensitive optical diffraction tomography

Amirhossein Saba,* Joowon Lim, Ahmed B. Ayoub, Elizabeth E. Antoine, and Demetri Psaltis

Optics Laboratory, École polytechnique fédérale de Lausanne, CH-1015, Lausanne, Switzerland
**Corresponding author: amirhossein.sabashirvan@epfl.ch*

Received 23 November 2020; revised 2 February 2021; accepted 4 February 2021 (Doc. ID 415343); published 12 March 2021

Polarization of light has been widely used as a contrast mechanism in two-dimensional (2D) microscopy and also in some three-dimensional (3D) imaging modalities. In this paper, we report the 3D tomographic reconstruction of the refractive index (RI) tensor using 2D scattered fields measured for different illumination angles and polarizations. Conventional optical diffraction tomography (ODT) has been used as a quantitative, label-free 3D imaging method. It is based on the scalar formalism, which limits its application to isotropic samples. We achieve imaging of the birefringence of 3D objects through a reformulation of ODT based on vector diffraction theory. The off-diagonal components of the RI tensor reconstruction convey additional information that is not available in either conventional scalar ODT or 2D polarization microscopy. Finally, we show experimental reconstructions of 3D objects with a polarization-sensitive contrast metric quantitatively displaying the true birefringence of the samples.

https://doi.org/10.1364/OPTICA.415343

1. INTRODUCTION

Polarization microscopy [1] is an imaging technique that exploits the birefringence contrast of the samples and has been extensively used in pathology and diagnosis of some diseases, such as squamous cell carcinoma [2]. This microscopy modality has been studied intensively and has evolved during many years. Birefringence is observed in collagen, muscle tissue, tendons, retina nerves, fibroblasts, starch, and biological samples containing fibrous structures in polarization-sensitive bright-field microscopy [3]. Nonlinear microscopy methods such as coherent anti-Stokes Raman scattering microscopy [4] and second-harmonic microscopy [5] have also been studied as polarization-sensitive techniques.

In quantitative two-dimensional (2D) polarization imaging, several works studied polarization-sensitive holography for birefringent samples [6–11]. The Oldenbourg group has developed a liquid-crystal-based polariscope method (LC-PolScope) [12,13] presenting 2D images of birefringence distribution. Regarding three-dimensional (3D) imaging techniques, polarization-sensitive optical coherence tomography has been thoroughly investigated for imaging birefringent samples [14–16]. Confocal florescence polarization microscopy has also been reported [17], and the LC-polariscope has been used together with a multi-focus grating to provide 2D birefringence images in multiple planes [18]. However, none of these methods yield a quantitative reconstruction of birefringence in 3D, and a quantitative, label-free, and 3D imaging method for polarization microscopy does not currently exist.

Optical diffraction tomography (ODT), on the other hand, is a quantitative, label-free, and 3D imaging method that reconstructs the distribution of the refractive index (RI) values of a sample using multiple-angle-measured scattered fields. Emil Wolf's work in 1969 [19] was a landmark in the establishment of ODT, in which he proposed the Fourier diffraction theorem using the Born approximation. Subsequently, ODT has undergone intensive research in terms of experimental and algorithmic viewpoints [20–22]. For example, Wolf's method was used with the Rytov approximation to improve reconstructions [23]. Experimental aspects such as illumination rotation [24,25], sample rotation [26], and wavelength scanning [27] have been thoroughly investigated. Phase-contrast tomography of cells inside the microfluidic channels is also presented [28,29]. Iterative schemes have been proposed to compensate for the missing spatial frequency information due to the limited numerical aperture [30], and nonlinear forward models with optimization have been implemented to address multiple-scattering samples [31–33].

Previous studies on ODT reconstruction are based on the scalar Helmholtz equation and, therefore, are limited to isotropic samples. The 3D scalar RI distribution of a sample reveals useful morphological and biological information; however, as mentioned earlier, many biological and non-biological samples are birefringent, and their RI cannot be represented with a scalar parameter. In this work, we study polarization-sensitive ODT for birefringent samples and reconstruct the 3D distribution of the RI tensor. The Jones formalism [34] is used throughout this paper. The Jones matrix of the sample has been measured holographically for multiple illumination angles. We then derive the tensorized

version of Wolf's method and use it for direct tomographic reconstructions. Synthetic data are generated using the vectorial beam propagation method (V-BPM), and they are used to guide the experiments in polarization-sensitive ODT. Finally, we discuss the 3D polarization-based contrast metric to be presented as the 3D map of the sample showing its birefringence.

2. METHODOLOGY

A. Theory

The importance of considering polarization for ODT is highlighted in Fig. 1. We applied conventional ODT reconstruction using the Rytov approximation for a cornstarch granule, which is a birefringent sample [35]. In two experiments, the illumination beam had +45° and −45° linear polarization states with respect to the X axis in the XY coordinate. We measured the X-polarized light of the scattered light using a conical scan at 180 equally spaced illumination angles with a 30° angle with respect to the Z axis. In Figs. 1(a)–1(c), we show the YX profiles of the 3D reconstructions for the two different illumination cases (+45° and −45° linear polarizations) followed by the difference between them. This figure clearly demonstrates the importance of considering polarization in ODT. The Y components of the two incident polarizations are both coupled to the measured X polarization only for an anisotropic sample such as the corn kernel used in this experiment. The opposite sign of the Y components in the incident light are responsible for the difference between the reconstructions in Figs. 1(a) and 1(b). On the other hand, when the sample is isotropic, there is no light coupling between the X and Y polarizations. As a result, independently of the sign of the Y-polarized light in the +45° and −45° states, the reconstructions will be same. This has been shown in Figs. 1(d)–1(f) for a 4.5 μm diameter polystyrene bead, which is immersed in silicon oil.

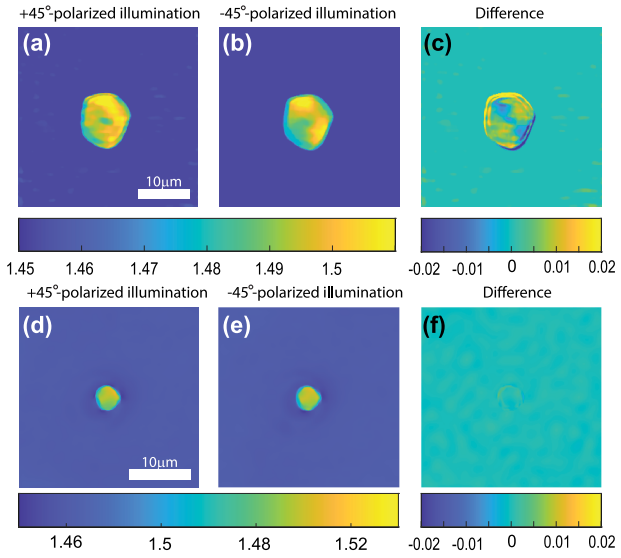

Fig. 1. YX profiles of the conventional Rytov ODT reconstructions. On the top we have the reconstruction of the cornstarch kernel, and multiple scattered fields were measured in the X polarization when the illumination beam was (a) +45°-polarized and (b) −45°-polarized. (c) The difference between the two reconstructions of cornstarch. Then, we have the reconstruction for an isotropic polystyrene bead when the illumination beam was (d) +45°-polarized and (e) −45°-polarized. (f) The difference between the two reconstructions of the polystyrene bead.

The input and output field vectors and their relationship can be presented in the Jones vectors and Jones matrix, $\vec{E}^{\text{out}} = \bar{\bar{J}}\,\vec{E}^{\text{in}}$, in which $\vec{E}^{\text{out}}$ and $\vec{E}^{\text{in}}$ are the fields after and before the sample (Jones vectors) and the linear transformation between two vectors is represented by the Jones matrix, $\bar{\bar{J}}$. The Jones formalism represents a relationship between the complex fields, and its components are also complex values. As a result, holography or iterative phase retrieval methods are necessary to reconstruct the complex scattered fields.

We derive the vectorial form of the Helmholtz equation to study the interaction of light with the sample. At the same time, we introduce the "scattering potential tensor," a quantity that is an extension of the scalar scattering potential that we use as a contrast metric when we form the 3D image of the birefringent sample. The integral solution of the vectorial Helmholtz equation can be obtained under the Born approximation (see Section 1 of Supplement 1). We consider a case when the sample is illuminated with the illumination beam vector $\vec{E}^{\text{illum}}$ and consider the corresponding holographically recorded scattered field vector $\vec{E}^{s}$,

$$\vec{E}^{s}(r) = \int \bar{\bar{G}}(r, r') \times \bar{\bar{V}}(r') \times \vec{E}^{\text{illum}}(r')\mathrm{d}^3 r', \tag{1}$$

where $\bar{\bar{G}}$ is the Green's function (tensor) and $\bar{\bar{V}} = n_0 k_0^2 \bar{\bar{\delta}} n/2\pi$ is the scattering potential (tensor), which is defined in terms of the quantity $\bar{\bar{\delta}} n$, which we refer to as the RI tensor. The RI tensor is defined in Supplement 1, and it is discussed further in Section 3. Since the sample is assumed to be immersed in a liquid, the background is isotropic and homogeneous. Therefore, the Green's function is a diagonal tensor, with the diagonal elements of the scalar case.

The RI tensor, and correspondingly the scattering potential tensor, and Jones matrix are, in general, 3 × 3 tensors. As a result, we need three independent polarization states for $\vec{E}^{\text{illum}}$ to reconstruct the full 3 × 3 Jones matrix for each projection. However, since the polarization state of the incident light is perpendicular to its wave vector, we can only have two independent polarization states for each illumination angle. Therefore, we calculate the scattering potential using 2 × 2 tensors by neglecting the Z component. The validity of this approximation and the resulting error are discussed in Section 3 of Supplement 1.

Now, each element of the scattering potential tensor can be calculated with Wolf's method, considering that $E^{\text{illum}}(r') = \tilde{E}^{\text{illum}} \times e^{j\vec{k}^{\text{in}}\cdot r'}$:

$$\bar{\bar{V}}(k_x - k_x^{\text{in}}, k_y - k_y^{\text{in}}, k_z - k_z^{\text{in}}) = \frac{k_z}{2\pi j}\mathcal{F}_{2\text{D}}\left\{\begin{pmatrix} E_{x1}^{s} & E_{x2}^{s} \\ E_{y1}^{s} & E_{y2}^{s} \end{pmatrix}\begin{pmatrix} \tilde{E}_{x1}^{\text{illum}} & \tilde{E}_{x2}^{\text{illum}} \\ \tilde{E}_{y1}^{\text{illum}} & \tilde{E}_{y2}^{\text{illum}} \end{pmatrix}^{-1}\right\}(k_x, k_y). \tag{2}$$

Equation (2) is derived in Supplement 1. After taking the 2D Fourier transform from the scattered fields, we shift them in the Fourier domain based on $\vec{k}^{\text{in}}$ and then fill the Fourier domain of the scattering potential by adding the spectra for all the incident angles. At the end, we take the inverse 3D Fourier transform to reconstruct the scattering potential tensor in the spatial domain. All of these operators are linear and can be considered equivalent to the Wolf transform [19] operating on each of four elements of the tensor independently using the Born approximation (see also Section 1

of Supplement 1). Alternatively, the Rytov approximation can be used, where we consider $\vec{E}^t$ as $\overline{\overline{[e^{\varphi}]}} \times \vec{E}^{\text{illum}}$. In this case, we will have

$$\begin{pmatrix} E^s_{xx} & E^s_{xy} \\ E^s_{yx} & E^s_{yy} \end{pmatrix} = \left(\overline{\overline{[e^{\varphi}]}} - \mathbb{1}\right) \times \begin{pmatrix} E^{\text{illum}}_{x1} & E^{\text{illum}}_{x2} \\ E^{\text{illum}}_{y1} & E^{\text{illum}}_{y2} \end{pmatrix}, \tag{3}$$

which leads to

$$\bar{\bar{\varphi}} = \text{logm}\left(\mathbb{1} + \begin{pmatrix} E^s_{x1} & E^s_{x2} \\ E^s_{y1} & E^s_{y2} \end{pmatrix} \begin{pmatrix} E^{\text{illum}}_{x1} & E^{\text{illum}}_{x2} \\ E^{\text{illum}}_{y1} & E^{\text{illum}}_{y2} \end{pmatrix}^{-1}\right). \tag{4}$$

logm is the matrix logarithm, and $\bar{\bar{\varphi}}$ is the complex phase tensor whose imaginary part should be unwrapped [36]. Same as the scalar case, Rytov approximation is based on the first-order Taylor expansion, where $\bar{\bar{E}}^s / \bar{\bar{E}}^{\text{illum}} \approx \text{logm}(\mathbb{1} + \bar{\bar{E}}^s / \bar{\bar{E}}^{\text{illum}})$. The reconstructed scattering potential $\bar{\bar{V}}$ can be found by applying the Wolf transform, separately on each of the components of $\bar{\bar{\varphi}} e^{jk^{\text{in}} \cdot r}$.

The formulation described above is based on the scattered E^s and illumination E^{illum} fields immediately before and after the sample. However, in ODT, we illuminate the sample with different projections, from different angles (experimentally implemented using a galvomirror, as explained in the next subsection). As a result, with fixed input polarization of light in a fixed coordinate frame (here, XYZ experiment coordinates), changing the illumination angle changes the polarization of the illumination field. In this situation, by tilting the beam, the polarization of light will remained unchanged in the meridional plane (the plane containing the ray, and the optical axis, here z), and it can be expressed in the XYZ Cartesian coordinate, using a rotational matrix [37]:

$$\begin{pmatrix} E^{\text{illum}}_x \\ E^{\text{illum}}_y \\ E^{\text{illum}}_z \end{pmatrix} = \bar{\bar{R}} \times \begin{pmatrix} E^{\text{in}}_x \\ E^{\text{in}}_y \\ E^{\text{in}}_z \end{pmatrix}, \tag{5a}$$

$$\bar{\bar{R}} = \begin{pmatrix} \sin^2\phi(1-\cos\theta) + \cos\theta & -\sin\phi\cos\phi(1-\cos\theta) & \cos\phi\sin\theta \\ -\sin\phi\cos\phi(1-\cos\theta) & \cos^2\phi(1-\cos\theta) + \cos\theta & \sin\phi\sin\theta \\ -\cos\phi\sin\theta & -\sin\phi\sin\theta & \cos\theta \end{pmatrix}. \tag{5b}$$

The parameters θ and ϕ are indicated in Fig. 2(b). The absolute value of the nine components of the rotational matrix is shown in Fig. 2(a). The same matrix maps the complex measured fields to the complex scattered field, right after the sample, to compensate for the angular demagnification in the 4F system from the sample to the CCD, including the water-dipping objective and the lens L4,

$$\vec{E}^s = \bar{\bar{R}} \times \vec{E}^m. \tag{6}$$

Here, $\vec{E}^m$ is the field vector, whose last component is always zero, as the perpendicular component to the camera cannot be measured. There are other contributions in the polarization change of the light, such as light refraction in the air-glass and glass-water interface, and also oblique illumination to the polarizer. These are discussed in Supplement 1.

In Eqs. (2) and (4), we are working with the cross-polarized light, $E^s_{yx}/E^{\text{illum}}_x$. We have zero intensity values in these terms when there is no scattering and/or birefringence, which leads to a random background phase values. As an example, the phase of this cross-polarized term is shown in Supplement 1 (Fig. S7) for one illumination angle. The random background phase values make the unwrapping and calibration challenging. To overcome this issue, we can note the fact that Eq. (1) is linear with respect to $\bar{\bar{E}}^{\text{illum}}$. As a result, we can get scattered fields in the XY coordinate, if we illuminate with any pair of perpendicular polarization states, such as the 45° ab coordinate system as shown in Fig. 2(b). This way, when the input and output polarization states are not aligned, we do not have the intensity singularity problem. For instance, we present the phase of E^s_{xa} in Supplement 1 in comparison with the phase of cross-polarized light (Fig. S7). On this subject, based on the linearity of Eq. (1), 3D reconstructions can be performed using E^s_{xa}, E^s_{xb}, E^s_{ya}, and E^s_{yb}, and then converted to the XY RI tensor using the procedure discussed in the Section 4 of Supplement 1.

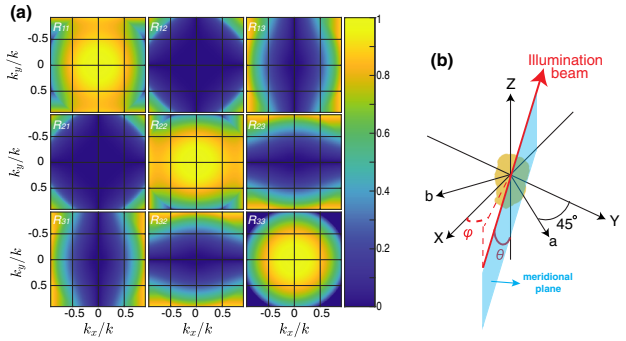

Fig. 2. (a) Rotational matrix described in Eq. (5), for polarization conversion of an oblique illumination. (b) Definition of the coordinate system.

B. Experimental Setup

The polarization-sensitive holographic tomography system used to acquire experimental data is shown in Fig. 3(a). The signal and reference arms are combined in an off-axis configuration to record holograms at different illumination angles. The source is a 488 nm CW fiber coupled laser diode, which is collimated and split into the signal and reference arms with a beam splitter. The polarization of the signal arm is controlled with a half-wave plate (HW1) and a polarizer (P1). The illumination angle is scanned with a double-axis galvomirror. We consider two arbitrary polarization states for our illuminations, +45° and −45°, namely a and b, according to Fig. 2(b). Thanks to a 4F system consisting of a lens, L1, and a 60× dry objective as the condenser, the position of the beam is fixed on the sample while scanning the angle. The imaging of the sample on a CCD camera is done using another 4F system with a water-dipping 60× objective and a tube lens (L2). The polarization of the reference arm is aligned at 45° with respect to the X and Y axis to get the same intensity of reference light for interference with both polarizations. The signal beam for which the polarization is chosen using an analyzer, in two states of X and Y, is combined with the reference arm by a beam splitter. We measure four holograms totally and reconstruct the complex fields E_{xa}, E_{ya}, E_{xb}, and E_{yb}, where in E_{ij}, j indicates the incident polarization and i indicates the output polarization. For calibration purposes (as the illumination fields are not perfect plane waves), we measure E^{illum}_{ij} in the absence of the sample. In Fig. 3(b), the cross-polarized light

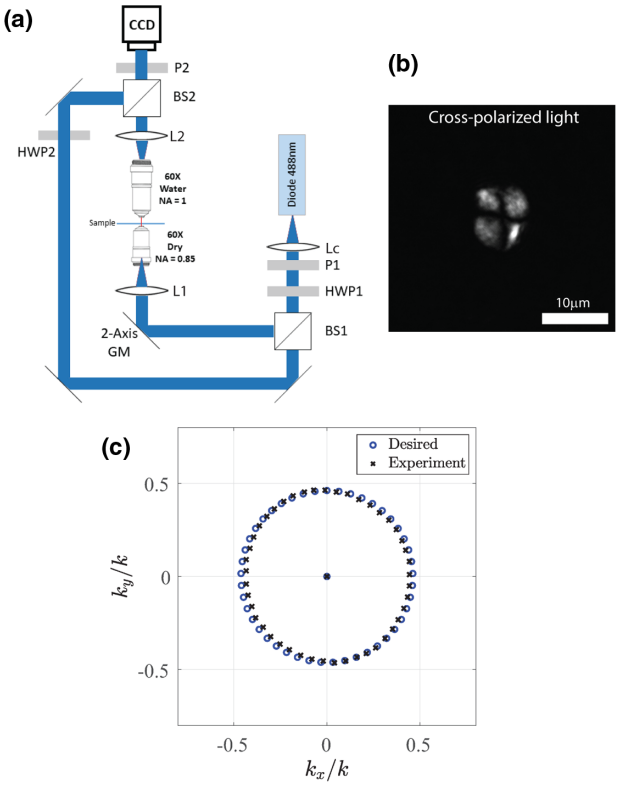

Fig. 3. (a) Schematic of the polarization-sensitive holography setup has been used to get vectorial scattered fields for different illumination angles. (b) Cross-polarized light can be measured from a cornstarch granule when illuminated with a Y-polarized light. (c) Illumination pattern in the k-space: circles are the desired pattern, and crosses are the experimental pattern that is measured using Fourier analysis of the holograms.

due to the birefringence of the sample is shown in the absence of the reference beam, for the cornstarch granule. Figure 3(c) shows the illumination pattern in the k-space. The desired pattern is shown with circles. The experimental pattern is achieved using the Fourier map of the hologram and is shown with crosses. For some angles, it is slightly different from the desired pattern, due to the imperfections of the galvo mirror. When we find the illumination pattern using our holograms, the $\bar{\bar{R}}$ matrix of Eq. (2a) is calculated by sampling the pattern in Fig. 2(a) with the points in Fig. 3(c).

3. RESULTS AND DISCUSSION

A. Numerical Phantom

We tested the proposed 3D reconstruction method using synthetic data generated using a numerical forward model, the split-step V-BPM, in order to numerically calculate the 2D projections. The accuracy of the reconstruction method was assessed by comparing the reconstruction with the known index tensor distribution of the digital phantom. The forward model, V-BPM, is derived in Section 2 of Supplement 1. The basic idea of this model is to propagate light slice-by-slice by dividing a 3D sample into multiple 2D slices. The relationship between two subsequent slices can be described by Eq. (8). To be specific, we can calculate the vector field, $\vec{E}(z+dz)$, by propagating the field from the previous slice, $\vec{E}(z)$, followed by the phase and amplitude modulation caused by the inhomogeneity and the birefringence of the medium, $\overline{\overline{\delta n}}(x, y, z)$:

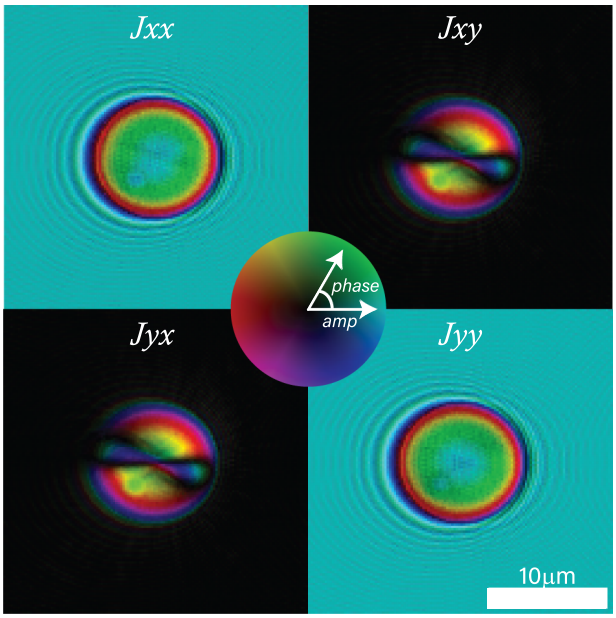

Fig. 4. Complex Jones matrix calculated for a birefringent digital phantom with an illumination angle of $\theta = 25°$ and $\phi = 0°$. The synthetic measurements were generated using the V-BPM. In order to visualize the complex values, brightness shows the amplitude, and the color-code shows the phase of each Jones matrix component.

$$\vec{E}(z+dz) = \text{expm}\left(\frac{jk_0\overline{\overline{\delta n}}(z)dz}{\cos\theta}\right) \times \mathcal{F}^{-1}\left\{e^{-j\frac{k_x^2+k_y^2}{k+k_z}dz} \times \mathcal{F}\{\vec{E}(z)\}\right\}, \quad (7)$$

where dz is the step size, expm is the matrix exponential applied on the RI tensor, $\overline{\overline{\delta n}}$, $\mathcal{F}$ is the 2D Fourier transform, and k_x, k_y, $k_z = \sqrt{k^2 - k_x^2 - k_y^2}$ represent the spatial frequencies in each direction.

Using the V-BPM, the scattered vector fields are calculated for a digital phantom with $+45°$-polarized and $-45°$-polarized input fields. The rotational matrix described in Eqs. (5) and (6) is also considered. Four complex calculated fields, normalized to the input vector fields to give the Jones matrix, are shown in Fig. 4, for an illumination with $\theta = 25°$ and $\phi = 0°$, where θ and ϕ are defined in Fig. 2(b). Ninety projections are calculated keeping θ but varying ϕ. Then, we use these data for our reconstruction. The reconstruction process is similar to what we use for the experimental data. We reconstruct based on the Rytov approximation, and we convert the reconstructions to get n_{xx}, n_{yx}, n_{xy}, and n_{yy}. In Fig. 5, we present the reconstruction of n_{xx} and n_{yx}, and compare them with the ground-truth. We can see the underestimation and elongation along the optical axis, which is due to the missing spatial frequencies, similarly to the scalar ODT [30]. The full reconstruction of the tensor is shown in Supplement 1 and is discussed in detail. We define the mean square error (MSE) as $\text{MSE} = \|n^{\text{reconstruction}} - n^{\text{ground-truth}}\|^2 / \|n^{\text{ground-truth}}\|^2$ to perform a quantitative evaluation on the 3D reconstruction of the RI tensor with respect to the ground-truth. Based on our calculation on the data of Fig. 5, for n_{xx}, the MSE of the reconstruction at the plane of focus ($z = 0$ μm) is 0.104, and the total MSE is 0.381. On the other hand, for n_{yx}, the MSE of the reconstruction at the plane of focus is 0.317, and the total MSE is 0.451. The larger value of the

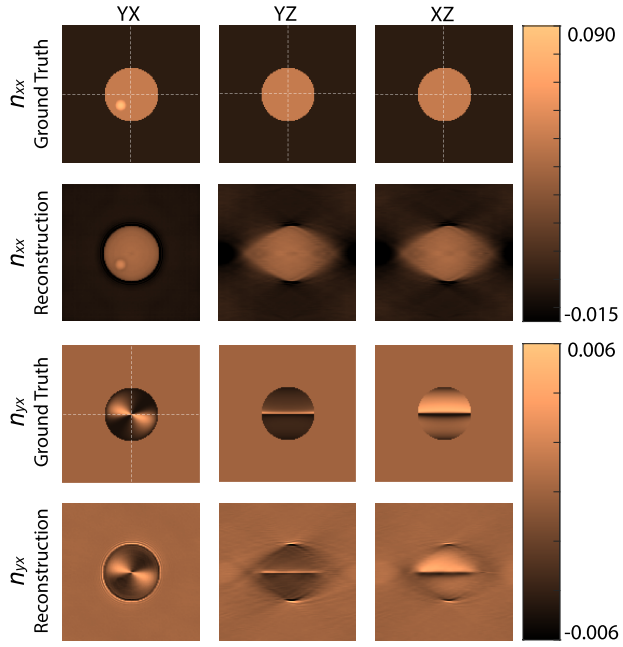

Fig. 5. Reconstruction of the digital birefringent phantom using the Rytov approximation. First and second rows show YX, YZ, and XZ profiles of the ground-truth, and reconstruction of n_{xx}, respectively. Third and fourth rows show the same profiles for n_{yx}. Full tensor ground-truth and reconstructions are presented in Supplement 1.

total MSE is due to the fact that the Rytov reconstruction is always better in the plane of best focus.

B. Experiment

As proof of concept of our method, we first demonstrate our experimental setup by reconstructing the 3D RI tensor of a cornstarch granule. Cornstarch granules, which exhibit a simple birefringent structure, were suspended in silicone oil ($n_0 = 1.43$) and placed between two #1 glass coverslips for imaging. Here, in order to overcome the phase unwrapping problem in the presence of experimental noise, we use the idea of nonaligned input and output polarization. As a result, the sample is illuminated from different angles with $+45°$-polarized and $-45°$-polarized light, and we measure the X and Y components of the output field. Then, the reconstructions are processed to get the RI tensor in the XY coordinate system. A 3D total-variation (TV) denoising algorithm as defined in Eq. S33 of Supplement 1 with a regularization parameter of $\lambda = 2 \times 10^{-3}$ is used on the final reconstructions to diminish the coherent noise due to the unwanted reflections on the final reconstructions [38]. This TV algorithm is only for denoising purposes, is directly applied on the final images, and does not compensate the missing-cone problem. This issue is elaborated in Section 7 of Supplement 1. Results are shown in Fig. 6, where we can see four different components of the RI tensor, n_{xx}, n_{xy}, n_{yx}, and n_{yy}, in 3D. As it can be seen in the off-diagonal terms of the RI tensor, there are some azimutally varying structures that came from the amylopectin crystalline structures growing radially in corn, from its hilum. The diagonal RI components are bereft of this information, the same as the conventional scalar ODT.

Next, we investigate the viability of using our method for more complex anisotropic samples. We present a case study using *ex vivo* mouse muscle tissue, a well-studied example of a naturally birefringent tissue [39]. Striated muscle fiber cells in mammals contain

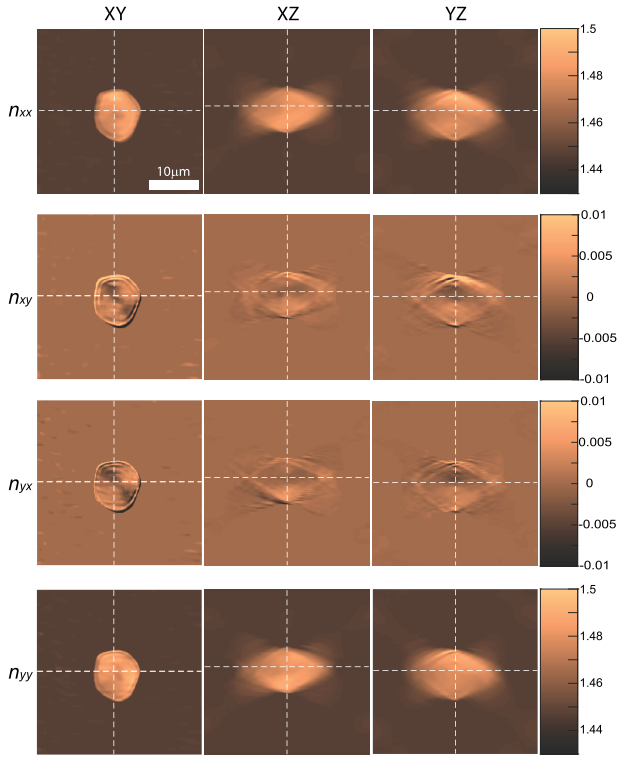

Fig. 6. YX, XZ, and YZ profiles of the 3D RI tensor reconstruction of the cornstarch granule.

repeated longitudinally connected units known as sarcomeres, which are periodically organized into substructures including A-bands (anisotropic) and I-bands (isotropic). As the characteristic length scale of A- and I- bands is on the order of 1 μm, muscle tissue is well-suited for a demonstration of our method. Fresh *ex vivo* mouse muscle was cryo-embedded, sectioned into 20 μm slices, mounted on a coverslip with water immersion, and imaged under the same conditions as the previous experiment. The cross-polarized image is shown in Fig. S6 of Supplement 1. The regularization parameter in the 3D TV denoising algorithm for this muscle tissue is $\lambda = 0.8 \times 10^{-3}$ and is applied directly on the final 3D RI tensor reconstructions. Figure 7 shows YX slices from the 3D reconstruction of the RI tensor at three different depths. The section of the tissue sample shown here consists of two *en face* muscle fiber cells that are separated by a thin layer of connective tissue. The inset in Fig. 7, providing a closer look at n_{xy} term, indicates that this measurement could be used to extract quantitative morphological data about the sarcomere structure. Some evidence of these structures is also visible in the images of n_{xx}, which can be attributed to the fact that both quantities are related to the local mass density.

C. Coordinate-Invariant Polarization-Sensitive Contrast Metrics

The RI tensor, which contains n_{xx}, n_{xy}, n_{yx}, and n_{yy} components, depends on the coordinate system, which has been chosen arbitrarily. One can change the coordinate system and get a new RI tensor. For example when the coordinate system matches with the optical axes of the sample, we will have a diagonal RI tensor. As a result, the values of off-diagonal components in the RI tensor do not directly indicate the inherent birefringence of the sample. A sample with a

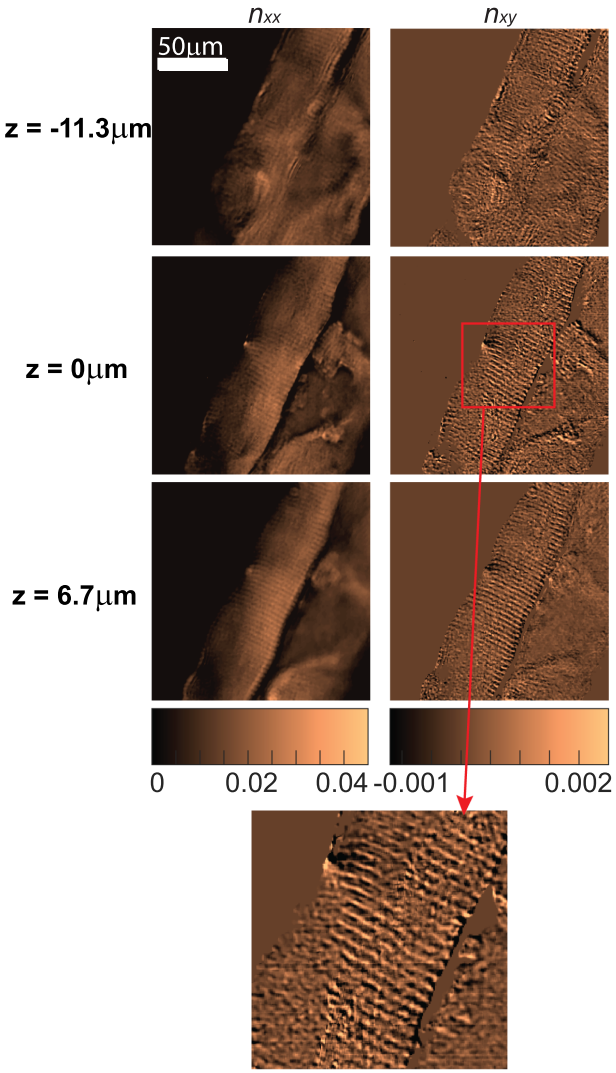

Fig. 7. YX profiles of the 3D reconstructions of the RI tensor components, n_{xx} and n_{xy}, for a 20 μm thick muscle tissue in three different depths. The inset shows a 2.5× magnified section of n_{xy} YX profile, which clarifies the sarcomere structure with A-bands and I-bands in one muscle fiber. A z-stack video is shown in Visualization 1.

larger value of n_{yx} in a particular location may be less birefringent than another sample with a smaller n_{yx} depending on the orientation of the local optical axis with respect to the laboratory coordinates.

To solve this issue, we can study the eigenvalue decomposition of the RI tensor. The eigenvalues of a matrix are invariant under any unitary transformation, such as the coordinate rotation. We can consider the local phase modulation tensor in Eq. (7), $\exp(jk_0 dz\overline{\overline{\delta n}})$, that the electric field vector experiences as it propagates through a step dz. This step is a linear operator, and its eigenvectors and eigenvalues can be readily calculated. We use the *difference* in the phases of these eigenvalues (δ^1 and δ^2) as the contrast metric since they convey the local retardation, independently of orientation. It has been shown in Section 2 of Supplement 1 that δ is directly related to the eigenvalues of the RI tensor $\mu_n^{1,2}$:

$$\delta = \delta^1 - \delta^2 = k_0 dz(\mu_n^1 - \mu_n^2). \tag{8}$$

The phase retardation, $\delta(x, y, z)$, is a 3D scalar quantity, which is invariant under any rotation of the coordinate system in the XY plane. In Fig. 8, we present the calculated 3D phase retardation for the cornstarch granule. The YX profiles of the reconstructed n_{xy} and phase retardation are compared in Figs. 8(a) and 8(b). We can see that these two contrast metrics can show different shapes depending on the local orientation of the optical axis. A 3D rotating rendering of the phase retardation rendered with the Icy platform [40] is shown in Visualization 2, and a 3D view of that can be seen in Fig. 8(c). It should be mentioned that eigenvalue and eigenvector characterization of the RI tensor is the key point to quantify the parameters of anisotropicity with a physical meaning. Each component of the RI tensor, by itself, does not convey information about the local birefringence or the local direction of the fibrous structures of the sample. However, the birefringence can be calculated as the difference in the eigenvalues of the RI tensor ($\mu_n^1 - \mu_n^2$), and the slow-axis orientation of the sample can be calculated by eigenvectors of the RI tensor. These parameters (that have been shown and discussed in Section 6 of Supplement 1) are inherent properties of the sample and do not get affected by the orientation of the experimental coordinate.

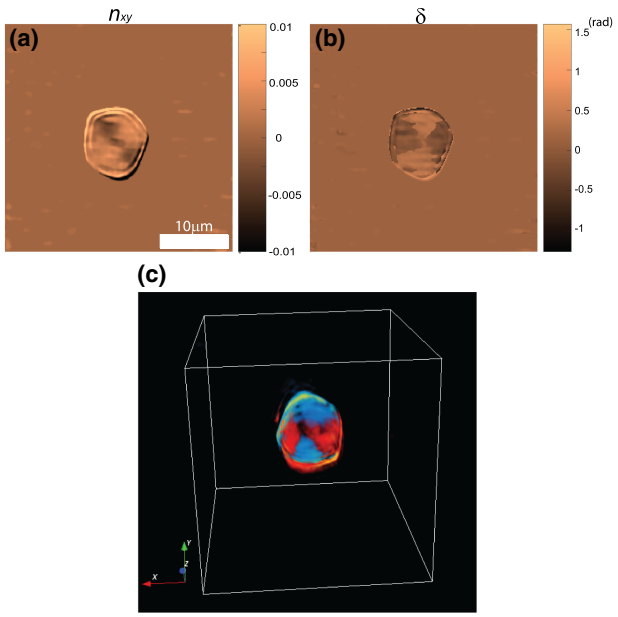

Fig. 8. Comparison between the YX profiles of the 3D reconstructions of (a) n_{xy} and (b) phase retardation for the cornstarch granule. A 3D rotating rendering of the phase retardation is presented in Visualization 2, and a 3D view of that is shown in (c).

4. CONCLUSION

In conclusion, we studied ODT in the anisotropic scenarios and showed how conventional ODT reconstruction can be different depending on the input polarization for a birefringent sample. We formulated the linear ODT for RI tensors, under the Rytov approximation, and evaluated with some numerical examples. In this numerical case, simulations were done with V-BPM, derived as the forward model. Using a polarization-sensitive holography setup, we presented 3D RI tensor reconstructions using multiple-angle vectorial scattered fields.

Our direct reconstruction method can be further improved by incorporating iterative reconstruction schemes along with nonlinear forward models, such as our V-BPM, and we expect to extend the previously developed learning tomography approaches for

isotropic samples to general anisotropic samples [31]. Polarization-sensitive ODT should be important for biological samples with fibrous structures to provide information about the biological details related with the birefringence of the sample and can be resolved in the off-diagonal components of the RI tensor or the 3D phase retardation.

Funding. Swiss National Science Foundation (514481).

Acknowledgment. The authors would like to thank EPFL Histology lab for helping to prepare the muscle tissue.

Disclosures. The authors declare no conflicts of interest.

Supplemental document. See Supplement 1 for supporting content.

REFERENCES

1. S. Inoué, "Polarization microscopy," Curr. Protoc. Cell Biol. **13**, 4–9 (2002).
2. P. Arun Gopinathan, G. Kokila, M. Jyothi, C. Ananjan, L. Pradeep, and S. Humaira Nazir, "Study of collagen birefringence in different grades of oral squamous cell carcinoma using picrosirius red and polarized light microscopy," Scientifica (Cairo) **2015**, 802980 (2015).
3. T. Wilson, R. Juškaitis, and P. Higdon, "The imaging of dielectric point scatterers in conventional and confocal polarisation microscopes," Opt. Commun. **141**, 298–313 (1997).
4. J.-X. Cheng, L. D. Book, and X. S. Xie, "Polarization coherent anti-Stokes Raman scattering microscopy," Opt. Lett. **26**, 1341–1343 (2001).
5. G. Latour, I. Gusachenko, L. Kowalczuk, I. Lamarre, and M.-C. Schanne-Klein, "*In vivo* structural imaging of the cornea by polarization-resolved second harmonic microscopy," Biomed. Opt. Express **3**, 1–15 (2012).
6. T. Colomb, P. Dahlgren, D. Beghuin, E. Cuche, P. Marquet, and C. Depeursinge, "Polarization imaging by use of digital holography," Appl. Opt. **41**, 27–37 (2002).
7. T. Colomb, E. Cuche, F. Montfort, P. Marquet, and C. Depeursinge, "Jones vector imaging by use of digital holography: simulation and experimentation," Opt. Commun. **231**, 137–147 (2004).
8. X. Liu, B.-Y. Wang, and C.-S. Guo, "One-step Jones matrix polarization holography for extraction of spatially resolved Jones matrix of polarization-sensitive materials," Opt. Lett. **39**, 6170–6173 (2014).
9. S. Aknoun, P. Bon, J. Savatier, B. Wattellier, and S. Monneret, "Quantitative retardance imaging of biological samples using quadri-wave lateral shearing interferometry," Opt. Express **23**, 16383–16406 (2015).
10. B. Ge, R. Zhou, Y. Takiguchi, Z. Yaqoob, and P. T. So, "Single-shot optical anisotropy imaging with quantitative polarization interference microscopy," Laser Photon. Rev. **12**, 1800070 (2018).
11. Y. Jiao, M. E. Kandel, X. Liu, W. Lu, and G. Popescu, "Real-time Jones phase microscopy for studying transparent and birefringent specimens," Opt. Express **28**, 34190–34200 (2020).
12. M. Shribak and R. Oldenbourg, "Techniques for fast and sensitive measurements of two-dimensional birefringence distributions," Appl. Opt. **42**, 3009–3017 (2003).
13. M. I. Shribak and R. Oldenbourg, "Mapping polymer birefringence in three-dimensions using a polarizing microscope with oblique illumination," Proc. SPIE **5462**, 57–67 (2004).
14. J. F. De Boer, T. E. Milner, M. J. Van Gemert, and J. S. Nelson, "Two-dimensional birefringence imaging in biological tissue by polarization-sensitive optical coherence tomography," Opt. Lett. **22**, 934–936 (1997).
15. J. F. De Boer, C. K. Hitzenberger, and Y. Yasuno, "Polarization sensitive optical coherence tomography–a review," Biomed. Opt. Express **8**, 1838–1873 (2017).
16. C. K. Hitzenberger, E. Götzinger, M. Sticker, M. Pircher, and A. F. Fercher, "Measurement and imaging of birefringence and optic axis orientation by phase resolved polarization sensitive optical coherence tomography," Opt. Express **9**, 780–790 (2001).
17. B. S. DeMay, N. Noda, A. S. Gladfelter, and R. Oldenbourg, "Rapid and quantitative imaging of excitation polarized fluorescence reveals ordered septin dynamics in live yeast," Biophys. J. **101**, 985–994 (2011).
18. S. Abrahamsson, M. McQuilken, S. B. Mehta, A. Verma, J. Larsch, R. Ilic, R. Heintzmann, C. I. Bargmann, A. S. Gladfelter, and R. Oldenbourg, "Multifocus polarization microscope (MF-PolScope) for 3D polarization imaging of up to 25 focal planes simultaneously," Opt. Express **23**, 7734–7754 (2015).
19. E. Wolf, "Three-dimensional structure determination of semi-transparent objects from holographic data," Opt. Commun. **1**, 153–156 (1969).
20. F. Charrière, A. Marian, F. Montfort, J. Kuehn, T. Colomb, E. Cuche, P. Marquet, and C. Depeursinge, "Cell refractive index tomography by digital holographic microscopy," Opt. Lett. **31**, 178–180 (2006).
21. W. Choi, C. Fang-Yen, K. Badizadegan, S. Oh, N. Lue, R. R. Dasari, and M. S. Feld, "Tomographic phase microscopy," Nat. Methods **4**, 717–719 (2007).
22. D. Jin, R. Zhou, Z. Yaqoob, and P. T. So, "Tomographic phase microscopy: principles and applications in bioimaging," J. Opt. Soc. Am. B **34**, B64–B77 (2017).
23. K. Iwata and R. Nagata, "Calculation of refractive index distribution from interferograms using the Born and Rytov's approximation," Jpn. J. Appl. Phys. **14**, 379–383 (1975).
24. Y. Sung, W. Choi, C. Fang-Yen, K. Badizadegan, R. R. Dasari, and M. S. Feld, "Optical diffraction tomography for high resolution live cell imaging," Opt. Express **17**, 266–277 (2009).
25. Y. Cotte, F. Toy, P. Jourdain, N. Pavillon, D. Boss, P. Magistretti, P. Marquet, and C. Depeursinge, "Marker-free phase nanoscopy," Nat. Photonics **7**, 113–117 (2013).
26. S. Vertu, J. Flügge, J.-J. Delaunay, and O. Haeberlé, "Improved and isotropic resolution in tomographic diffractive microscopy combining sample and illumination rotation," Cent. Eur. J. Phys. **9**, 969–974 (2011).
27. P. Hosseini, Y. Sung, Y. Choi, N. Lue, Z. Yaqoob, and P. So, "Scanning color optical tomography (SCOT)," Opt. Express **23**, 19752–19762 (2015).
28. F. Merola, P. Memmolo, L. Miccio, R. Savoia, M. Mugnano, A. Fontana, G. D'ippolito, A. Sardo, A. Iolascon, A. Gambale, and P. Ferraro, "Tomographic flow cytometry by digital holography," Light Sci. Appl. **6**, e16241 (2017).
29. M. M. Villone, P. Memmolo, F. Merola, M. Mugnano, L. Miccio, P. L. Maffettone, and P. Ferraro, "Full-angle tomographic phase microscopy of flowing quasi-spherical cells," Lab Chip **18**, 126–131 (2018).
30. J. Lim, K. Lee, K. H. Jin, S. Shin, S. Lee, Y. Park, and J. C. Ye, "Comparative study of iterative reconstruction algorithms for missing cone problems in optical diffraction tomography," Opt. Express **23**, 16933–16948 (2015).
31. U. S. Kamilov, I. N. Papadopoulos, M. H. Shoreh, A. Goy, C. Vonesch, M. Unser, and D. Psaltis, "Learning approach to optical tomography," Optica **2**, 517–522 (2015).
32. J. Lim, A. B. Ayoub, E. E. Antoine, and D. Psaltis, "High-fidelity optical diffraction tomography of multiple scattering samples," Light Sci. Appl. **8**, 1–12 (2019).
33. J. Lim, A. B. Ayoub, and D. Psaltis, "Three-dimensional tomography of red blood cells using deep learning," Adv. Photon. **2**, 026001 (2020).
34. N. Ortega-Quijano and J. L. Arce-Diego, "Generalized Jones matrices for anisotropic media," Opt. Express **21**, 6895–6900 (2013).
35. S. Shin, K. Lee, Z. Yaqoob, P. T. So, and Y. Park, "Reference-free polarization-sensitive quantitative phase imaging using single-point optical phase conjugation," Opt. Express **26**, 26858–26865 (2018).
36. J. M. Bioucas-Dias and G. Valadao, "Phase unwrapping via graph cuts," IEEE Trans. Image Process. **16**, 698–709 (2007).
37. M. R. Foreman and P. Török, "Computational methods in vectorial imaging," J. Mod. Opt. **58**, 339–364 (2011).
38. L. I. Rudin, S. Osher, and E. Fatemi, "Nonlinear total variation based noise removal algorithms," Physica D **60**, 259–268 (1992).
39. A. Douplik, G. Saiko, I. Schelkanova, and V. Tuchin, "The response of tissue to laser light," in *Lasers for Medical Applications* (Elsevier, 2013), pp. 47–109.
40. F. De Chaumont, S. Dallongeville, N. Chenouard, N. Hervé, S. Pop, T. Provoost, V. Meas-Yedid, P. Pankajakshan, T. Lecomte, Y. Le Montagner, T. Lagache, A. Dufour, and J.-C. Olivo-Marin, "Icy: an open bioimage informatics platform for extended reproducible research," Nat. Methods **9**, 690–696 (2012).